Monthly Notices of the ROYAL ASTRONOMICAL SOCIETY

MNRAS **514,** 1879–1885 (2022) https://doi.org/10.1093/mnras/stac1309
Advance Access publication 2022 May 12

Multiple photoionization for the 2p subshell in the iron atom

Sigitas Kučas,★ Aušra Kynienė, Šarūnas Masys and Valdas Jonauskas★
Institute of Theoretical Physics and Astronomy, Vilnius University, Saulėtekio av. 3, LT-10257 Vilnius, Lithuania

Accepted 2022 May 5. Received 2022 April 15; in original form 2022 February 23

ABSTRACT

Multiple photoionization is investigated for the 2p subshell in the iron atom. Study of the single photoionization with subsequent radiative and Auger cascade includes levels corresponding to the ground configuration. This work reveals that the quadruple photoionization dominates over other multiple-photoionization processes. Analysis of the partial photoionization cross sections to configurations of the produced ions shows that the excited long-lived configurations accumulate the main population of the Fe^{4+} ion. The main decay branches of the radiative and Auger cascade produced after a creation of the 2p subshell vacancy in the iron atom are identified. The ion yields for the photoionization and cascade obtained by considering level-to-level transitions are compared to the previous configuration average calculations.

Key words: atomic data – atomic processes – line: formation.

1 INTRODUCTION

Study of the interstellar medium (ISM) is critical in understanding the structure of the Galaxy and formation of stars. High resolution X-ray spectroscopy provides an important information about abundance of the constituent elements in the ISM. The multiphase structure characterized by gas, dust, and molecules can be determined through analysis of absorption lines and edges in the X-ray spectra. The interstellar absorption for the Fe $L_{2,3}$ edges was observed in the spectra of low mass X-ray binaries (LMXB) (Pinto et al. 2010, 2013). The overabundance of iron was found in LMXB 1826-238 (Pinto et al. 2010). It was determined that a significant fraction of neutral iron is formed in dust of the ISM. The Fe *L*-edge region was also analysed in the X-ray spectra of 24 galactic sources obtained from *Chandra* and *XMM–Newton* missions (Gatuzz et al. 2016). What is more, the lines of iron provide an important contribution to the spectra from active galactic nuclei (AGNs) (Wills, Netzer & Wills 1985; Boroson & Green 1992; Marinello et al. 2016; Onori et al. 2017; Ilić et al. 2020; Oknyansky et al. 2020). The previous level-to-level results of the multiple photoionization were presented for the K shell of iron atom and Fe^{2+} ion (Kučas et al. 2020a, 2021). However, modelling of ionization balance in photoionized plasma requires photoionization cross sections for all ions and their shells.

In continuation of our earlier work on multiple photoionization of the Fe atom and ions (Kučas et al. 2020a, 2021), here we investigate the multiple photoionization produced by a creation of the 2p subshell vacancy in the Fe atom. Level-to-level study of the photoionization process is presented for all levels originating from the ground configuration of the Fe atom. Previously, an ion yield produced by radiative and Auger cascade was analyzed using configuration-average calculations (Kaastra & Mewe 1993). The cascades were investigated using energies obtained by Lotz (Lotz 1967, 1968). However, it was demonstrated (Schippers et al. 2017; Beerwerth et al. 2019; Kučas et al. 2019; Kučas, Drabužinskis & Jonauskas 2020b; Kučas et al. 2020a, 2021) that higher ionization stages were obtained in these calculations compared to the level-to-level analysis for the iron atom and ions because more Auger transitions were included in calculations by modifying energies of configurations with vacancies (Kaastra & Mewe 1993).

Photoemission of the atomic Fe was already experimentally and theoretically studied for the 2p subshell (Richter et al. 2004). But the results for produced ionization stages and cross sections, unfortunately, were not presented. Recently, the multiple photoionizations near *L*-edge of the Fe^{+}, Fe^{2+}, and Fe^{3+} ions were theoretically and experimentally investigated (Schippers et al. 2017; Beerwerth et al. 2019; Schippers et al. 2021). The PETRA III synchrotron light source was employed to measure cross sections of the multiple photoionization. The theoretical study of the multiple photoionization included the 2*p* subshell for Fe^{+} (Schippers et al. 2017) and Fe^{2+} (Schippers et al. 2021) ions while the 2s and 2p subshells were analysed for the Fe^{3+} ion (Beerwerth et al. 2019). Good agreements with experimental results were obtained in the most cases for the multiple-photoionization cross sections. Besides, Auger cascades following a creation of the L shell in the Fe^{2+} ion were investigated using the Dirac-Fock-Slater (DFS) approach (Kučas et al. 2019; Kučas et al. 2020b) with no multiple photoionization being taken into account. The multiple-photoionization process for photon energies above the ionization threshold of the K-shell vacancy was analysed for the iron atom (Kučas et al. 2021) and Fe^{2+} ion (Kučas et al. 2020a). The multiple-photoionization cross sections for the K-shell vacancy in the Fe atom and Fe^{2+} ion showed large dependence on the levels of the ground configuration. It should be noted that the cascade decay from the K shell produces higher ionization stages and requires to analyse at least by an order of magnitude more energy levels compared to the decay from the L-shell vacancy. The present work aims to fill a gap in the literature on the multiple photoionization for the 2p subshell in the iron atom. Calculations for the 2s subshell are on the way and will be published elsewhere.

★ E-mail: Sigitas.Kucas@tfai.vu.lt (SK); valdas.jonauskas@tfai.vu.lt (VJ)

We describe theoretical approach in Section 2. The multiple-photoionization cross sections, cascade decay, and ion yields are discussed in Section 3. In the final section, we summarize our results of the presented study.

2 THEORETICAL APPROACH

Atomic data such as energy levels, radiative and Auger transition probabilities are calculated using the Flexible atomic code (FAC) (Gu 2008), which implements DFS approach. The single-configuration approximation is used in the study. The electric dipole transitions are investigated in the radiative decay process.

The multiple photoionization is analysed for photon energies above the ionization energy of the 2p subshell of the Fe atom:

$$\mathrm{Fe}\ 1s^2 2s^2 2p^6 3s^2 3p^6 3d^6 4s^2 + h\nu \rightarrow \mathrm{Fe}^+ 1s^2 2s^2 2p^5 3s^2 3p^6 3d^6 4s^2 + e. \quad (1)$$

This study does not include ionization of the 2s subshell and K shell for the iron atom while the studied energy region covers ionization thresholds of these electrons. The multiple-photoionization process for the K shell of the iron atom was previously analysed by Kučas et al. (2021).

Cross sections of multiple photoionization are investigated for all 34 levels of the ground configuration of the Fe atom. The single photoionization from the 2p subshell (equation 1) is followed by radiative and Auger cascade which mainly leads us to higher ionization stages. The cascade decay is analysed for 73 configurations (Fe^+: 5, Fe^{2+}: 13, Fe^{3+}: 18, Fe^{4+}: 20, Fe^{5+}: 17 configurations). These configurations correspond to 21151 energy levels: Fe^+: 522, Fe^{2+}: 2012, Fe^{3+}: 5577, Fe^{4+}: 7619, Fe^{5+}: 5421.

The single photoionization cross sections are defined by relation:

$$\sigma_{if}^{\mathrm{PI}}(\omega) = \frac{2}{3}\pi\alpha\frac{\omega}{g_i}S_{if}, \quad (2)$$

where α is the fine structure constant, ω is a photon energy, g_i is the statistical weight of the initial bound state, and S_{if} is the generalized line strength for initial i and final f states. The generalized line strength is written through submatrix element of the electric dipole operator:

$$S_{if} = \sum_{\kappa J_T} |\langle \Psi_i \| \boldsymbol{D} \| \Psi_f, \kappa; J_T \rangle|^2. \quad (3)$$

Here, $\boldsymbol{D} = \sum_i \boldsymbol{r}_i$ (the sum is over the number of electrons) is the electric dipole operator, Ψ_i and Ψ_f are wavefunctions for the initial and final states, respectively; κ is the relativistic quantum number of the free electron, J_T is the total angular momentum.

The transfer of population n_{if} from the level i to the level f is expressed through probabilities of radiative and Auger transitions:

$$n_{if} = n_i \frac{A_{if}}{\sum_k A_{ik}^r + \sum_m A_{im}^a}, \quad (4)$$

where n_i is the population of the level i, A_{if} is the probability of the radiative or Auger transition, A_{ik}^r and A_{im}^a are the probabilities of the radiative and Auger transitions, respectively. The sum in the denominator determines the total decay probability through the radiative and Auger transitions for the level i. The total population transferred to the level f is calculated by summing over the initial levels i in equation (4). The same approach was previously applied to investigate the radiative and Auger cascades for various elements using configuration average (Jonauskas, Karazija & Kučas 2000; Jonauskas et al. 2003) and level-to-level (Palaudoux et al. 2010; Jonauskas, Kučas & Karazija 2011; Kučas et al. 2019; Kučas et al. 2020a) calculations. It is worthwhile noting that the higher moments of spectra were incorporated in the study for transitions among average energies of configurations to mimic the widths of energy levels (Kučas & Karazija 1993) and Auger spectra (Kučas et al. 1995). This led to a production of the higher ionization stages compared to the ordinary configuration-average calculations for the cascades. The multiple Auger transitions, where more than one electron is emitted from atomic system, are not considered in this work since it is expected that probability of a such process would be by an order of magnitude lower compared to ordinary Auger transitions (Müller et al. 2015). It has been revealed that the multiple Auger transitions can be analysed as ejection of the bound electrons by leaving Auger electron (Zhou, Ma & Qu 2016; Müller et al. 2018).

Cross sections of multiple photoionization are also investigated for levels of the ground configuration of the Fe atom taking initial population corresponding to their statistical weights. The ion yield (product charge-state fraction) for the photoionization process can be expressed by equation:

$$B_q^{\mathrm{PI}}(\omega) = \frac{\sigma_q(\omega)}{\sigma(\omega)}. \quad (5)$$

Here, the cross sections of the multiple photoionization are defined by relation:

$$\sigma_q(\omega) = \sum_{if} g_i \sigma_{if}^{\mathrm{PI}}(\omega) B_{fq}, \quad (6)$$

where B_{fq} is the ion yield for the radiative and Auger cascade from the level f of the Fe^+ ion with the 2p subshell vacancy to charge state q; $g_i = 2J_i + 1$. It should be noted that $\sum_q B_{fq} = 1$. The total photoionization cross section is obtained by taking the sum over q in equation (6):

$$\sigma(\omega) = \sum_q \sigma_q(\omega) = \sum_{if} q_i \sigma_{if}^{\mathrm{PI}}(\omega). \quad (7)$$

Therefore, this leads us to the statistically weighted single-photoionization cross-section. In a similar way, the ion yield for the photoionization from the level i can be written as:

$$B_{iq}^{\mathrm{PI}}(\omega) = \frac{\sigma_{iq}(\omega)}{\sigma_i(\omega)}, \quad (8)$$

where

$$\sigma_{iq}(\omega) = \sum_f \sigma_{if}^{\mathrm{PI}}(\omega) B_{fq}. \quad (9)$$

The mean product-charge state for the cascade is determined by equation:

$$\bar{q}(\omega) = \sum_q q\, B_q^{\mathrm{PI}}(\omega). \quad (10)$$

This quantity defines an average charge state produced by multiple photoionization.

3 RESULTS

The single ionization threshold for the 2p subshell of the iron atom equals 713.3 eV. The energy of the Fe^+ $2p^5 3d^6 4s^2$ configuration is above the energy of the ground configuration ($3p^6$) of the Fe^{8+} atom which corresponds to 541.2 eV relative to the ground energy of the Fe atom. The energy levels of the ground configuration ($3p^5$) of the Fe^{9+} atom spans the energy region from 773.5 to 775.4 eV. The energy levels of the Fe^+ $2p^5 3d^6 4s^2$ configuration cover the energy region

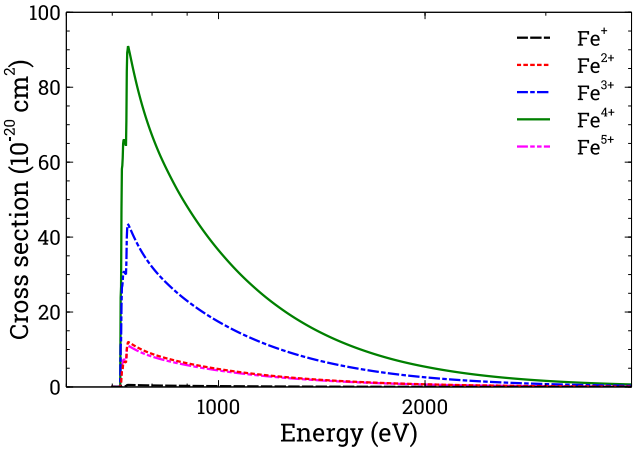

Figure 1. Cross sections for photoionization to the Fe^+, Fe^{2+}, Fe^{3+}, Fe^{4+}, and Fe^{5+} ions. The results are presented for the ground level of the iron atom.

from 719.5 eV to 247.3 eV (table of the energy levels is available at CDS data base website). It is worth to note that the ionization thresholds obtained using the DFS approach and single-configuration approximation are slightly lower compared to data given by the National Institute of Standards and Technology (NIST) (Kramida et al. 2021). Previous studies demonstrated that this discrepancy does not affect the results for the cascade decay (Kučas et al. 2019; Kučas et al. 2020a,b, 2021) or ionization by electron impact (Kynienė, Masys & Jonauskas 2015; Jonauskas 2018; Koncevičiūtė et al. 2018; Jonauskas et al. 2019).

The multiple-photoionization cross sections for the ground level of the iron atom are displayed in Fig. 1. Energy levels and their indexes of the ground configuration of the Fe atom are presented in Table 1. The states of the Fe^+ – Fe^{5+} ions are produced in the photoionization process. The quadruple-photoionization cross sections are larger than the ones of the triple photoionization approximately by a factor of two. The maximal value of the cross sections for the double and pentuple photoionization reaches $\sim 1.2 \times 10^{-19}$ cm^2. The single-photoionization cross sections are by two orders of magnitude lower compared to the quadruple-photoionization cross sections. It should be noted that peak of the quadruple photoionization cross sections is ∼20 eV above the single ionization threshold for the 2p subshell. This could be attributed to the fact that all energy levels of the Fe^+ $2p^5 3d^6 4s^2$ configuration are reached from the ground level by photoionization process employing a photon with energy corresponding to the peak of the cross sections. Besides, the energy levels of the Fe^+ $2p^5 3d^6 4s^2$ configuration span a region of ∼28 eV.

The similar situation is obtained for the multiple-photoionization cross sections from the highest level of the ground configuration of the iron atom (Fig. 2). The quadruple-photoionization cross sections also prevail for this level. On the other hand, the cross sections to Fe^{4+} are ∼10% higher for the ground level compared to the highest level of the ground configuration. What is more, difference among peak values of the quadruple-photoionization cross sections from the different levels of the ground configuration is ∼14%.

The partial photoionization cross sections from the ground level of the Fe atom to configurations of the Fe^{4+} ion are shown in Fig. 3. The cross sections to states of the Fe^{4+} $3d^3 4s$ configuration provide main contribution for the Fe^{4+} ion. The radiative decay from the states of the Fe^{4+} $3d^3 4s$ configuration to the ground configuration is forbidden by selection rules of the electric dipole transitions.

Table 1. Theoretical (DFS) energy levels (in eV) of the $3d^6 4s^2$ configuration of iron atom compared to the NIST data. The closed subshell $4s^2$ is not presented in the designation of the levels. The total angular momentum quantum numbers of the corresponding subshells are presented in parenthesis. Energies are presented relative to the ground energy.

i	Level	Term	NIST	DFS
0	$3d^3_{3/2}3d^3_{5/2}(9/2)4$	^5D	0.000	0.000
1	$3d^3_{3/2}3d^3_{5/2}(9/2)3$	^5D	0.052	0.060
2	$3d^2_{3/2}(2)3d^4_{5/2}(4)2$	^5D	0.087	0.102
3	$3d^1_{3/2}3d^5_{5/2}1$	^5D	0.110	0.129
4	$3d^2_{3/2}(2)3d^4_{5/2}(2)0$	^5D	0.121	0.142
5	$3d^3_{3/2}3d^3_{5/2}(9/2)6$	^3H	2.404	2.381
6	$3d^2_{3/2}(2)3d^4_{5/2}(4)5$	^3H	2.433	2.413
7	$3d^2_{3/2}(2)3d^4_{5/2}(4)4$	^3H	2.453	2.436
8	$3d^2_{5/2}2$	^3P	2.279	2.599
9	$3d^2_{5/2}4$	^3F	2.559	2.733
10	$3d^3_{3/2}3d^3_{5/2}(3/2)3$	^3F	2.588	2.768
11	$3d^1_{3/2}3d^5_{5/2}1$	^3P	2.424	2.781
12	$3d^3_{3/2}3d^3_{5/2}(3/2)2$	^3F	2.609	2.793
13	$4s^2_{1/2}0$	^3P	2.484	2.854
14	$3d^3_{3/2}3d^3_{5/2}(9/2)5$	^3G	2.949	3.030
15	$3d^1_{3/2}3d^5_{5/2}4$	^3G	2.990	3.087
16	$3d^2_{3/2}(2)3d^4_{5/2}(2)3$	^3G	3.018	3.112
17	$3d^2_{3/2}(2)3d^4_{5/2}(4)6$	^1I	3.634	3.595
18	$3d^2_{3/2}(2)3d^4_{5/2}(2)4$	^1G	3.695	3.801
19	$3d^2_{3/2}(2)3d^4_{5/2}(2)1$	^3D	3.635	3.942
20	$3d^2_{5/2}2$	^3D	3.640	3.944
21	$3d^3_{3/2}3d^3_{5/2}(9/2)3$	^3D	3.642	3.964
22	$3d^3_{3/2}3d^3_{5/2}(3/2)0$	^1S	–	4.432
23	$3d^1_{3/2}3d^5_{5/2}2$	^1D	4.294	4.759
24	$3d^3_{3/2}3d^3_{5/2}(3/2)3$	^1F	–	5.512
25	$3d^2_{5/2}0$	^3P	–	6.492
26	$3d^2_{3/2}(2)3d^4_{5/2}(0)2$	^3F	–	6.509
27	$3d^3_{3/2}3d^3_{5/2}(5/2)3$	^3F	–	6.528
28	$3d^2_{3/2}(0)3d^4_{5/2}(4)4$	^3F	–	6.530
29	$3d^3_{3/2}3d^3_{5/2}(5/2)1$	^3P	–	6.553
30	$3d^2_{3/2}(0)3d^4_{5/2}(2)2$	^3P	–	6.675
31	$3d^3_{3/2}3d^3_{5/2}(5/2)4$	^1G	–	7.361
32	$3d^2_{3/2}(0)3d^4_{5/2}(2)2$	^1D	–	9.978
33	$3d^2_{3/2}(0)3d^4_{5/2}(0)0$	^1S	–	12.884

The cross sections to the ground configuration of the Fe^{4+} ion are approximately by a factor of three lower compared to the first excited configuration of the ion. Attention should be paid to the fact that the $3p^5 3d^5$ configuration has negligible contribution to the cross sections of Fe^{4+} in comparison to $3d^3 4s$ configurations: lower by five orders of magnitude.

Ion yields of photoionization from all levels of the ground configuration for the Fe^{2+} – Fe^{4+} ions are presented in Figs 4–6. The ion yields are shown at photon energies of 800 eV. The yield for the Fe^{2+} ion varies within a range of ∼7% and the minimal value of ∼7.5% corresponds to the ground level of the iron atom (Fig. 4). It can be seen that variation of the ion yields for Fe^{3+} is within 1.5% (Fig. 5). The largest ion yield for photoionization is obtained for the

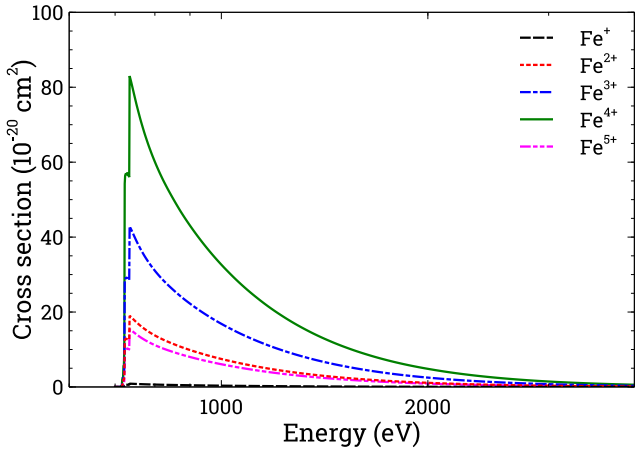

Figure 2. Cross sections for photoionization to the Fe^{+}, Fe^{2+}, Fe^{3+}, Fe^{4+}, and Fe^{5+} ions. The results are presented for the highest level of the ground configuration of the iron atom.

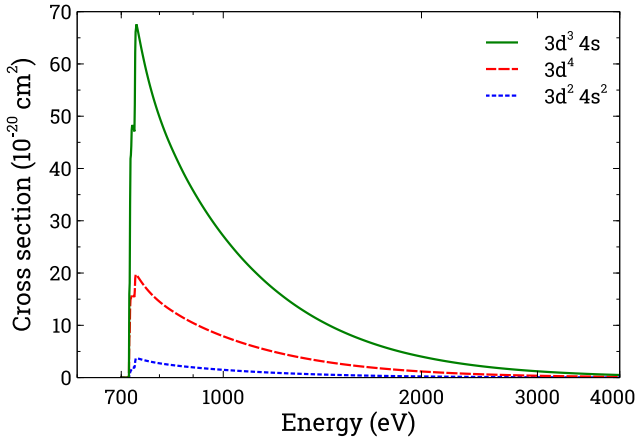

Figure 3. Cross sections for photoionization to configurations of the Fe^{4+}. The results are presented for the ground level of the iron atom.

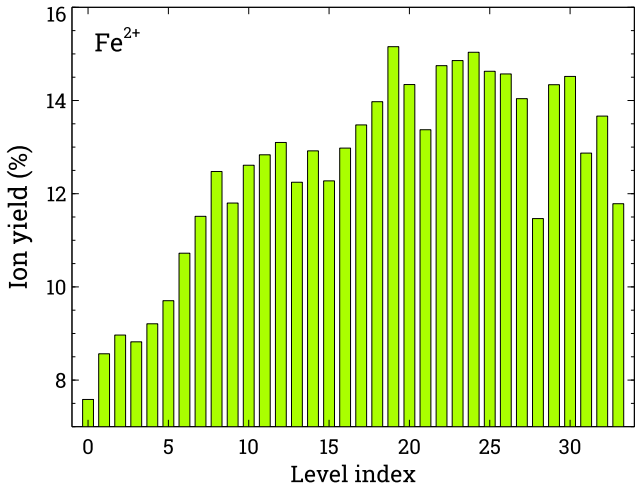

Figure 4. The ion yield of the 2p subshell photoionization for Fe^{2+} from the levels of ground configuration of the iron atom at photon energy of 800 eV.

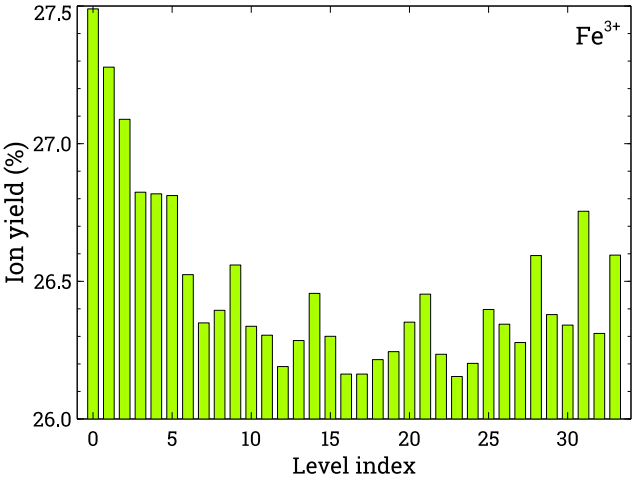

Figure 5. The same as Fig. 4 but for Fe^{3+}.

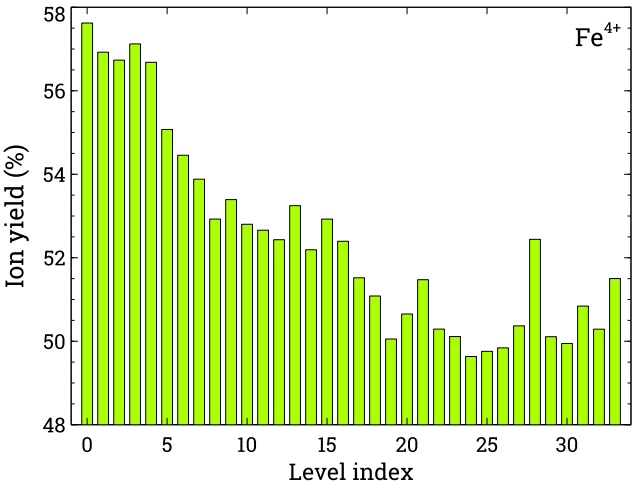

Figure 6. The same as Fig. 4 but for Fe^{4+}.

ground level of the iron atom and the lowest value is obtained for the level with index 24. The similar situation is seen for the yield of the Fe^{4+} ion (Fig. 6). The ground level dominates over other levels of the Fe $3d^64s^2$ configuration. However, the wider variation of the ion yield (∼8%) is obtained in this case compared to Fe $^{3+}$. What is more, the highest level of the ground configuration produces the highest yield for photoionization (not presented here) for the Fe^{5+} ion (∼9.5%) compared to the ground level (∼7%).

Multiple-photoionization process is considered as the 2p subshell photoionization followed by a cascade decay. The produced Fe^{+} $2p^53d^64s^2$ configuration has 180 energy levels. Decay branches for the Fe^{+} $2p^53d^64s^2$ configuration are presented in Figs 7–10. The populations of the levels of the Fe^{+} $2p^53d^64s^2$ configuration correspond to their statistical weights. The strongest branch of the cascade leads us to states of the Fe^{4+} ion: Fe^{+} $2p^53d^64s^2$ $\xrightarrow{46\%}$ Fe^{2+} $3p^43d^64s^2$ (Fig. 7) $\xrightarrow{41\%}$ Fe^{3+} $3p^53d^44s^2$ (Fig. 8) $\xrightarrow{37\%}$ Fe^{4+} $3d^34s$ (Fig. 9). This explains the largest partial quadruple-photoionization cross sections to the Fe^{4+} $3d^34s$ configuration (Fig. 3). The second strongest branch populates states of the Fe^{3+} ion: Fe^{+} $2p^53d^64s^2$ $\xrightarrow{25\%}$ Fe^{2+} $3p^53d^54s^2$ (Fig. 7) $\xrightarrow{21\%}$ Fe^{3+} $3d^34s^2$ (Fig. 8). The decay of the produced configurations to the energetically lower lying configurations is restricted by selection rules for the electric dipole

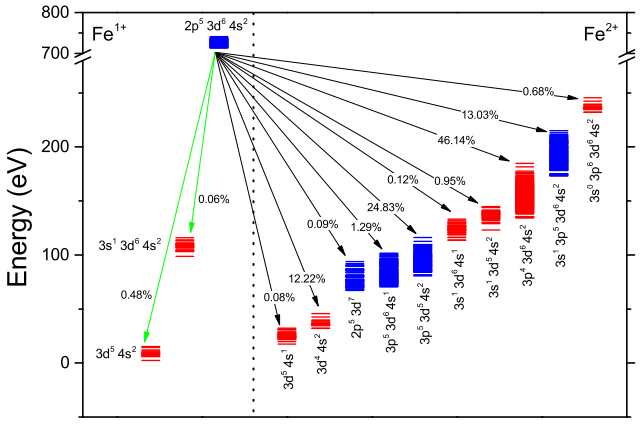

Figure 7. The decay paths of cascade following 2p inner-shell ionization of iron atom: configurations of Fe^{+} and Fe^{2+}. The population of the states of the Fe^{+} $2p^53d^64s^2$ configuration corresponds to their statistical weights. The populations transferred by radiative (green arrows) and Auger (black arrows) transitions are shown in per cents. The even and odd parity configurations are presented by red and blue colours, respectively.

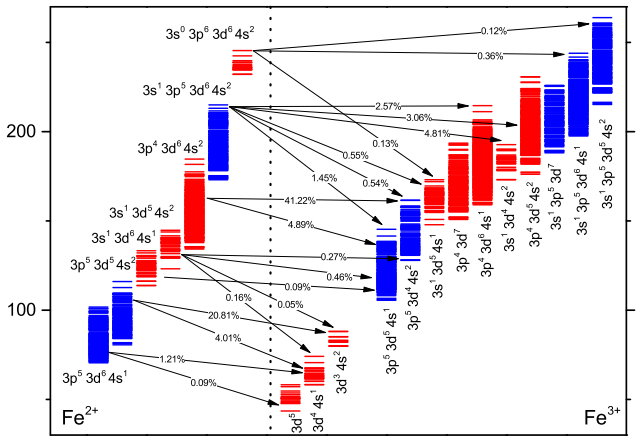

Figure 8. The decay paths of cascade following 2p inner-shell ionization of iron atom: configurations of Fe^{2+} and Fe^{3+}. The notations are the same as in Fig. 7.

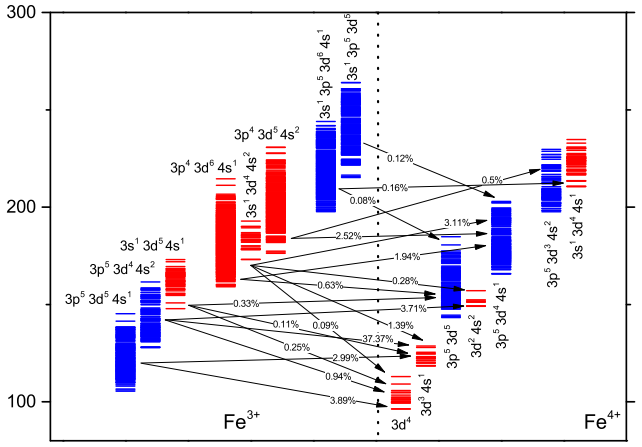

Figure 9. The decay paths of cascade following 2p inner-shell ionization of iron atom: configurations of Fe^{3+} and Fe^{4+}. The notations are the same as in Fig. 7.

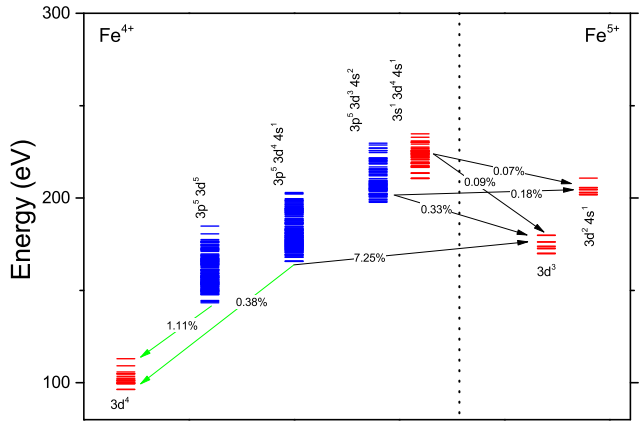

Figure 10. The decay paths of cascade following 2p inner-shell ionization of iron atom: configurations of Fe^{4+} and Fe^{5+}. The notations are the same as in Fig. 7.

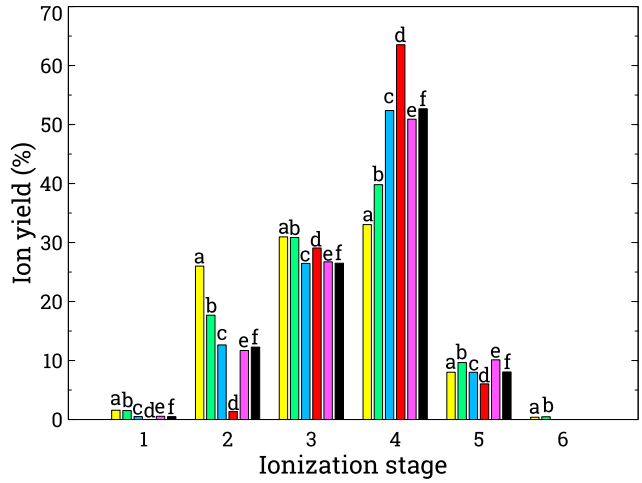

Figure 11. The ion yields produced by cascade decay: a (yellow) – results from configuration-average calculations for the L_2 shell (Kaastra & Mewe 1993), b (green) - results from configuration-average calculations for the L_3 shell (Kaastra & Mewe 1993), c (blue) – data for subconfigurations with the initial population corresponding to statistical weights, d (red) and e (magenta) – decay from the lowest and the highest levels of the Fe^{+} $2p^53d^64s^2$ configuration, respectively, f (black) – the ion yield of photoionization (equation 5).

transitions. The states of the Fe^{5+} ion are primarily populated by the Fe^{4+} $3p^53d^44s \xrightarrow{7\%} Fe^{5+}$ $3d^3$ transition (Fig. 10). The population of the Fe^{4+} $3p^53d^44s$ configuration (Fig. 9) mainly arrives from Fe^{3+} $3p^43d^64s$ (2%), Fe^{3+} $3s3d^44s^2$ (3%), and Fe^{3+} $3p^43d^54s^2$ (3%). Interestingly, the Fe^{2+} $3s3p^53d^64s^2$ configuration with total population of 13% (Fig. 7) populates the states of these three configurations (Fig. 8): Fe^{3+} $3p^43d^64s$ (3%), Fe^{3+} $3p^43d^54s^2$ (3%), and Fe^{3+} $3s3d^44s^2$ (5%).

Ion yields generated by a cascade decay from the 2p subshell of the Fe atom are shown in Fig. 11. Results for the lowest and highest levels of the $2p^53d^64s^2$ configuration of the Fe^{+} ion are presented along side with data from calculations for the statistically average population of the subconfigurations. In addition, the previous configuration-average calculations for the $2p_{1/2}$ and $2p_{3/2}$ subshells are shown (Kaastra & Mewe 1993). The yield for the Fe^{4+} ion is the largest for all presented data. It can be seen that the previous results (Kaastra & Mewe 1993) overestimate production of the Fe^{2+} ion

and underestimate the yield for the Fe^{4+} ion compared to the current data. Moreover, these configuration-average calculations show small population for the Fe^{6+} ion which is not obtained in our study. This could be due to the fact that the previous calculations included additional decay channels by modifying energies of configurations with inner-shell vacancies (Kaastra & Mewe 1993). The similar results for the higher ionization stages compared to the previous calculations were also obtained for other Fe ions (Schippers et al. 2017; Kučas et al. 2020a, 2021; Schippers et al. 2021). It should be noted that the study for transitions among the subconfigurations is in a good agreement to the level-to-level results. The ion yield obtained for the subconfigurations is between results provided from the lowest and highest levels of the Fe^+ $2p^53d^64s^2$ configuration (Fig. 11).

The ion yield for the photoionization is also compared to the ion yield from radiative and Auger cascade in Fig. 11. This corresponds the statistical population of the levels of the ground configuration for the Fe atom (equation 5). The ion yield for the photoionization is in a quite good agreement for the ion yield obtained for the radiative and Auger cascade corresponding to the statistically average population of the subconfigurations of the Fe^+ $2p^53d^64s^2$ configuration. And it is no surprise, since all levels originating from the ground configuration of the iron atom contribute to the ion yield in the photoionization process. This leads to the population of all levels of the Fe^+ $2p^53d^64s^2$ configuration and this population can be close to the statistical one. It is worth to note that mean product-charge state for the photoionization equals ∼3.6 and is slightly lower to the highest ion yield for the photoionization.

Interestingly, radiative and Auger cascade from the Fe^{3+} $2p^53d^6$ configuration reached levels of the Fe^{6+} ion (Kučas et al. 2020b). That is by three ionization stages higher compared to the initial one. In this study, the levels of the Fe^{5+} ion are reached from the Fe^+ $2p^53d^64s^2$ configuration. This means that the highest ionization stage produced by the radiative and Auger cascade is higher by four compared to the initial one. This could be attributed to the fact that more electrons are above the 2p subshell for the Fe^+ ion compared to Fe^{3+}.

4 CONCLUSIONS

Multiple photoionization is investigated for the 2p subshell of the iron atom. The process is studied as single photoionization of the 2p subshell with subsequent decay through cascade of radiative and Auger transitions. The study demonstrates that the quadruple photoionization plays the main role among the multiple-photoionization channels. Furthermore, the states of the excited Fe^{4+} $3d^34s$ configuration are primarily populated in the photoionization process. The multiple-photoionization cross sections to the states of the $3d^34s$ configuration produce ∼80% of the total cross sections to the Fe^{4+} ion.

Ion yields of photoionization are investigated for every level of the ground configuration of the Fe atom. In addition, the ion yield is presented assuming the statistical population of all levels corresponding to the ground configuration. The variation of the yield of photoionization to the Fe^{4+} ion reaches ∼8% for the different levels of the ground configuration of the iron atom.

The main decay branches of radiative and Auger cascade following a creation of the 2p subshell vacancy in the Fe atom are identified. Investigation of the ion yield for the cascade shows that the previous configuration-average calculations (Kaastra & Mewe 1993) underestimated production of the Fe^{4+} ion and overestimated population of the Fe^{2+} ion compared to the level-to-level results. A quite good agreement is obtained for the population of the Fe^{5+} ions with configuration-average calculations (Kaastra & Mewe 1993).

The multiple-photoionization cross sections are provided online at the Centre de Données astronomiques de Strasbourg (CDS) website (http://cds.u-strasbg.fr/). For the sake of convenience, the partial photoionization cross sections to the configurations of the produced ions are also tabulated.

ACKNOWLEDGEMENTS

Part of the computations were performed on the High Performance Computing (HPC) cluster at the Institute of Theoretical Physics and Astronomy, Faculty of Physics, Vilnius University.

DATA AVAILABILITY STATEMENT

The results are available online at the CDS website (http://cds.u-strasbg.fr/).

REFERENCES

Beerwerth R. et al., 2019, ApJS, 887, 189
Boroson T. A., Green R. F., 1992, ApJS, 80, 109
Gatuzz E., García J. A., Kallman T. R., Mendoza C., 2016, A&A, 588, A111
Gu M. F., 2008, Can. J. Phys., 86, 675
Ilić D. et al., 2020, A&A, 638, A13
Jonauskas V., 2018, A&A, 620, A188
Jonauskas V., Karazija R., Kučas S., 2000, J. Electron Spectrosc. Relat. Phenom., 107, 147
Jonauskas V. et al., 2003, J. Phys. B: At. Mol. Opt. Phys., 36, 4403
Jonauskas V., Kučas S., Karazija R., 2011, Phys. Rev. A, 84, 053415
Jonauskas V. et al., 2019, Phys. Rev. A, 100, 062701
Kaastra J. S., Mewe R., 1993, A&AS, 97, 443
Koncevičiūtė, J. Koncevičiūtė, S. Kučas, Masys Š., A. Kynienė, Jonauskas V., 2018, Phys. Rev. A, 97, 012705
Kramida A., Ralchenko Yu., Reader J., 2021, NIST ASD Team 2021, NIST Atomic Spectra Database (ver. 5.8). National Institute of Standards and Technology, Gaithersburg, MD
Kučas S., Karazija R., 1993, Phys. Scr., 47, 754
Kučas S., Karazija R., Jonauskas V., Aksela S., 1995, Phys. Scr., 52, 639
Kučas S., Drabužinskis P., Kynienė A., Masys Š., Jonauskas V., 2019, J. Phys. B: At. Mol. Opt. Phys., 52, 225001
Kučas S., Kynienė A., Masys Š., Jonauskas V., 2020, A&A, 643, A46
Kučas S., Drabužinskis P., Jonauskas V., 2020, Atom. Data Nucl. Data, 135, 101357
Kučas S., Kynienė A., Masys Š., Jonauskas V., 2021, A&A, 654, A74
Kynienė A., Masys Š., Jonauskas V., 2015, Phys. Rev. A, 91, 062707
Lotz W., 1967, J. Opt. Soc. Am., 57, 873
Lotz W., 1968, J. Opt. Soc. Am., 58, 915
Marinello M., Rodríguez-Ardila A., Garcia-Rissmann A., Sigut T. A. A., Pradhan A. K., 2016, ApJ, 820, 116
Müller A. et al., 2015, Phys. Rev. Lett., 114, 013002
Müller A. et al., 2018, Phys. Rev. A, 97, 013409
Oknyansky V. L. et al., 2020, MNRAS, 498, 718
Onori F. et al., 2017, MNRAS, 464, 1783
Palaudoux J. et al., 2010, Phys. Rev. A, 82, 043419
Pinto C., Kaastra J. S., Costantini E., de Vries C., 2010, A&A, 521, A79
Pinto C., Kaastra J. S., Costantini E., de Vries C., 2013, A&A, 551, A25
Richter T., Godehusen K., Martins M., Wolff T., Zimmermann P., 2004, Phys. Rev. Lett., 93, 023002
Schippers S. et al., 2017, ApJ, 849, 5
Schippers S. et al., 2021, ApJ, 908, 52
Wills B. J., Netzer H., Wills D., 1985, ApJ, 288, 94
Zhou F., Ma Y., Qu Y., 2016, Phys. Rev. A, 93, 060501

SUPPORTING INFORMATION

Supplementary data are available at *MNRAS* online.

Please note: Oxford University Press is not responsible for the content or functionality of any supporting materials supplied by the authors. Any queries (other than missing material) should be directed to the corresponding author for the article.

This paper has been typeset from a TEX/LATEX file prepared by the author.